Contents lists available at ScienceDirect

Chemical Engineering Science

journal homepage: www.elsevier.com/locate/ces

Optimizing fluid mixing in channel flow using wall-mounted flexible structures

Gaurav Singh[a,*], Arahata Senapati[a], Leixin Ma[c], Arnab Atta[d] and Rajaram Lakkaraju[e]

[a] Advanced Technology and Development Centre, Indian Institute of Technology Kharagpur, West Midnapore, 721302, W.B., India
[c] Department of Mechanical Engineering, Arizona State University, Tempe, 85281, Arizona, USA
[d] Department of Chemical Engineering, Indian Institute of Technology Kharagpur, West Midnapore, 721302, W.B., India
[e] TuRbulent Interfaces And Dispersion (TRIAD) Group, Department of Mechanical Engineering, Indian Institute of Technology Kharagpur, West Midnapore, 721302, W.B., India

ARTICLE INFO

Keywords:
fluid mixing
fluid structure interaction
flow transition
flexible structures
vortex generation
periodic flow
mixing performance

ABSTRACT

Fluid mixing in channel flows is a critical process in various industries, from chemical engineering to food processing. In our study, we focused on a passive mixing method by utilizing flexible wall-mounted plates in a channel of height h at various Reynolds numbers Re to investigate mixing performances. The channel flow, we examined, involved a scalar field with two initially separated concentration fields which upon fluid-structure-scalar interaction induce agitation and results in the intermixing of the two fields. We have varied the positions of two wall mounted plates, separated by distance $d/h = 0 - 2$, from each other to form different flow obstructing configurations in the channel, which result in different flow paths thereby affect fluid mixing and flow rate due the pressure head losses. Based on this value for cost analogy, we assessed mixing performance by using two primary metrics: the 'Mixing Index' and 'Head Loss' along the channel length. Our results showed that the setup with $d = 0$ offer highest mixing, early in the channel length but causes a large pressure drop. Whereas, single plate and other d/h configuration result in nearly similar level of mixing for $Re > 400$ but head losses increases with decreasing d/h. To determine the efficiency of different setup, we compared the equivalent mixing and head loss in an empty channel, (without any plate), and developed a comprehensive criterion called the "Coefficient of Performance" (CoP). This criterion allowed us to aggregate all cases and draw meaningful conclusions about the performance of different configuration and we found that $d/h = 1.5$ resulted in best mixing performance at low $Re(= 200)$. Whereas for $Re \geq 400$, a single plate in the channel offered best suited mixing performance among the rest cases. This study highlights the potential of designing the channel with flexible structures fluid mixing in channel flows, paving the way for more efficient industrial applications.

1. Introduction

Fluid mixing is a crucial process in various industries, such as fuel emulsification in petrochemicals, raw material blending in the food industry, and mixing chemical reagents (Peterwitz and Schembecker, 2021; Wang and Zhen, 2021; Núñez-Flores et al., 2020; Yeh et al., 2015). To achieve adequate mixing in channel flows, passive methods (like placing obstacles) and active methods (using externally powered actuators) can be employed. Passive methods, such as asymmetric grooves, rigid laminations, and serpentine channels, are simple and energy-efficient as they rely on the flow's inertia (Stroock et al., 2002; Nguyen and Wu, 2005; Squires and Quake, 2005; Kashid et al., 2011; Kang, 2015). Modifying the structural and dimensional aspects of mixing channels can improve mixing outcomes by inducing chaotic convective motions. For instance, Yang et al. (2015) developed a channel design inspired by the three-dimensional Tesla design, demonstrating a robust mixing index of 0.97 (where 0 meant no-mixing and 1 meant perfect-mixing case) within a Reynolds number range of 0.1 to 100.

Using flexible plates instead of rigid laminations involves complex interactions between hydrodynamic forces and structural responses, leading to various instabilities (Sadatoshi, 1968; Zhang et al., 2001; Watanabe et al., 2002; Eloy et al., 2008; Zhu and Peskin, 2002; Alben and Shelley, 2008). These instabilities trigger flow transition by generating eddies in the flow, causing significant improvement in fluid mixing (Singh and Lakkaraju, 2019a; Rips and Mittal, 2019;

*Corresponding author
**Principal corresponding author
thegauravonline@gmail.com (G. Singh); rajaram.lv@gmail.com (R. Lakkaraju)

Singh et al., 2024). The incorporation of various vortex-generating methods in mixing channels has emerged as a key approach in enhancing the mixing process (Ali et al., 2015; Khatavkar et al., 2007; Dadvand et al., 2019; Ali et al., 2016; Hsiao et al., 2014; Hosseini et al., 2021; van Loon et al., 2007; Eizadi et al., 2022). However, in the case of rigid geometry-based vortex generators, the vortex mainly concentrates in the small wake zone behind the obstacle, resulting in weak mixing near the channel wall, especially when the channel dimension greatly exceeds the obstacle size (Wang et al., 2020). A promising solution to this limitation is to employ flexible structures as vortex generators (Chen et al., 2020; Park et al., 2019; Saleh et al., 2019; Singh and Lakkaraju, 2019b; Zhao, 2020; Pfister and Marquet, 2020). A crucial method within this approach involves the placement of the obstructions in the flow that act as catalysts for flow agitation (Abdelhamid et al., 2021; Yadav et al., 2021; Jing and Zhan, 2022; Yu et al., 2017). Earlier works (Huera-Huarte and Gharib, 2011; Borazjani and Sotiropoulos, 2009; Wang and Zhou, 2018) have investigated the flow features when two flexible circular cylinders are placed one after the other. Wang and Zhou (2018) showed that the two structures act as a single body when placed at small separation, resulting in entirely different flow features when placed at a certain distance. Such strategies have also been used to enhance fluid mixing (Ward and Fan, 2015) and slug mitigation processes (Mehendale et al., 2018).

While experimental methods can measure pressure loss in channel flows, capturing erratic flow and plate motions is challenging, making numerical simulations a preferred approach. In context with the previous works on channel flows, we performed a two-dimensional numerical study to inspect fluid mixing in a channel flow containing two wall-mounted flexible plates mounted on opposite walls. We have systematically varied the position of the two plates to alter the flow features and quantify mixing using standard mixing metrics. We have also investigated the role of the flow Reynolds number that is best suited for efficient mixing conditions. Based on the strong coupling between the flow and the positioned structures, we aim to enhance mixing without causing significant pressure drop. We have focused our study on value (mixing) for cost (head loss) analogy and found the optimal configuration for mixing. In the following sections, we have discussed mathematical formulation, followed by our results and summary.

2. Mathematical formulation and computational setup

In Figure 1, we have shown a schematic of our model, a two-dimensional channel of height h and length $14h$ with two differently dyed fluid flows in the top half and the bottom half of the channel. The channel walls are fixed with flexible plates of length $l \approx 0.5h$ on the opposite wall. The upstream plate is placed at an entry length of $2h$ from the channel inlet, and the second flexible plate is separated at various distances, i.e., $d = 0h, 0.5h, 1.0h, 1.5h, 2.0h$. The thickness and width of each plate are $b = 0.05h$ and $w = 0.125h$ (into the plane), respectively. The chosen geometry is inspired by our previous work Singh and Lakkaraju (2019a); Jin et al. (2018), where flow transition past flexible plates mounted on the opposite channel walls is studied. A fully developed flow enters from the left on each dyed half as if the preceding flow had two separate channels with differently dyed fluids. The two flow streams in each half enter through the channel and interact with the wall-mounted structures, generating intricate flow features and thereby causing the mixing of the dyed fluids.

We have conducted a fluid-structure interaction numerical simulation for the mentioned domain using a partitioned approach, in which the fluid domain and the structure domain are numerically solved separately, and solutions are then exchanged to set iterative boundary conditions at the interface. We have considered fluid as Newtonian and incompressible, mathematically formulated by the Navier-Stokes equations. The linearly elastic structure is framed as solid equations of motion formulated using Arbitrary Lagrangian-Eulerian (ALE) framework Nguyen (2010); Slone et al. (2002); Campbell and Paterson (2011). The mass and momentum conservation expressions for the fluid and the structure are as follows,

$$\nabla \cdot \left[(\mathbf{u}_f - \mathbf{u}_m)\right] = 0,$$

$$\frac{\partial \mathbf{u}_f}{\partial t} + \left[(\mathbf{u}_f - \mathbf{u}_m)\cdot\nabla\right]\mathbf{u}_f = -\nabla p + \frac{1}{Re}\nabla^2\mathbf{u}_f,$$

$$\rho_s \frac{\partial^2 \mathbf{u}_s}{\partial t^2} = \nabla \cdot \boldsymbol{\sigma}_s$$

Here, $\mathbf{u}_f = (u_x, u_y)$ denotes the flow velocity, while $\mathbf{u}_m$ stands for the moving mesh velocity, and p represents the pressure, ρ_s symbolizes the structure density, $\mathbf{u}_s$ is the structural displacement, t is time, and the Cauchy stress tensor is represented by σ_s. $\frac{\partial}{\partial t}$ indicates the time derivative operator, and the spatial gradient is defined as $\nabla \equiv \left(\frac{\partial}{\partial x}, \frac{\partial}{\partial y}\right)$, with ∇^2 representing the Laplacian operator. The Reynolds number, Re, is defined as $Re = \overline{U}h/\nu_f$, where $\overline{U}$ is the mean inlet flow velocity and ν_f $(= \mu_f/\rho_f)$ is the fluid's kinematic viscosity. The subscripts $_f$, $_s$, and $_m$ refer to fluid, solid, and mesh, respectively.

When the plates deform under the fluid load, the strain rate is expressed as $\boldsymbol{\varepsilon}_s = \frac{1}{2}(\nabla\mathbf{u}_s + \nabla\mathbf{u}_s^T + \nabla\mathbf{u}_s \cdot \nabla\mathbf{u}_s^T)$. The relationship between the stress and strain tensors is given by $\boldsymbol{\sigma}_s = 2\mu_s\boldsymbol{\varepsilon}_s + \lambda(\nabla\cdot\mathbf{u}_s)\mathcal{I}$, where $\mu_s = \mathcal{E}/[2(1+\kappa)]$ and $\lambda = \kappa\mathcal{E}/[(1+\kappa)(1-2\kappa)]$ are Lame's constants. Here, κ denotes the Poisson's ratio, $\mathcal{E}$ is Young's modulus and $\mathcal{I}$ is the identity tensor of rank two. The transpose of a tensor is indicated by the superscript ^{T}. The interface condition ensures that flow stress and structural displacement influence each other through no-slip boundary conditions, and the mesh velocity is assumed to be equal to the structure velocity, i.e., $\mathbf{u}_m \equiv \frac{\partial \mathbf{u}_s}{\partial t}$.

In the presented setup, we have added a scalar concentration field ϕ to simulate the dyed fluids effect. The dye concentration is governed by advection-diffusion equation as,

$$\frac{\partial \phi}{\partial t} + (\mathbf{u}_f - \mathbf{u}_m) \cdot \nabla \phi = \frac{1}{Re \cdot Sc} \nabla^2 \phi,$$

where ϕ is the scalar concentration field ranging from 0 to 1, and $Sc = \nu_f / D$ is the Schimdt number with D as the mass diffusivity constant.

We used the finite volume method to solve the governing equations, employing a second-order accurate Euler-implicit scheme for temporal discretization and a second-order van-Leer TVD scheme for spatial discretization of convection terms. For diffusion terms, we applied a central differencing scheme with Gaussian integration. We maintained the Courant number below 0.2, calculated based on the local velocity magnitude, the integration time step, and the length of the computational cell. Our solution method involves predicting the interface displacement and computing the initial interface residual. This entails estimating the movement of the interface between the fluid and structure domains and determining the deviation from its initial position. After calculating the initial interface residual, the algorithm begins the fluid-structure interaction using a strongly coupled iterative procedure until the convergence criterion is achieved (Tukovic and Jasak, 2007; Campbell and Paterson, 2011). This iterative process is repeated under the Aitken dynamic relaxation approach until the desired tolerance level is achieved.

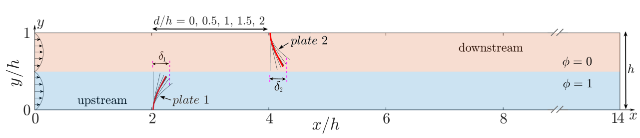

Figure 1: Schematic of a flow in a channel with a scalar concentration field ϕ, which is separated along the channel length in top half as $\phi = 0$ and bottom-half as $\phi = 1$. The channel walls consist of oppositely mounted flexible plates which bend in the streamwise direction when flow enters from the inlet (left). The inlet flow profile is considered fully developed separately for both top-half and bottom-half concentration field as if they enter in the domain from two different sources. Plate 1 and plate 2, each of height $0.5h$ are separated at different distances (d/h).

In our study, the characteristic velocity is denoted by $\overline{U}$, and the characteristic length is based on the flow gap between the wall and the anchored plate, specifically $(h - l) = 0.5h\ (= l)$. The dimensionless parameters include the Reynolds number $Re = \overline{U} l / \nu_f$, the density ratio ρ_s / ρ_f, and Cauchy number as the ratio of fluid inertia to elastic restoring force i.e. $Ca = \rho_f \overline{U}^2 h^3 b / \mathcal{E} I$, where $I = bw^3/12$ is the plate's area moment of inertia (Bagheri et al., 2012; Favier et al., 2015). Another critical parameter is the dimensionless gap between the plates, d/h. Our study primarily involves two time scales: (1) the plate's elasticity time scale, $\tau \sim 1/\sqrt{\mathcal{E} I / (\rho_s b w l^4)}$, and (2) the convective motion time scale, $T \sim l / v_\infty$. When τ / T is much less than 1, fluid inertia is negligible, and the plate oscillates at its natural frequency. Conversely, when τ / T is much greater than 1, fluid inertia dominates the plate's oscillations. Notably, τ and Ca are related through $\tau \sim \sqrt{(\rho_s w / \rho_f h)\, Ca}$. Given the significance of elastic restoring forces, we selected a small Ca value (≈ 0.015) to align with previous studies involving flexible silicone obstructions (Vandenberghe et al., 2004; Singh and Lakkaraju, 2019a). Our main objective is to examine fluid mixing by varying the inlet Reynolds number within the range $100 < Re < 3200$ and adjusting the plate separation gap from $0h$ to $2h$.

The inlet flow profile across the channel is designed to replicate a fully developed parabolic flow, similar to Poiseuille flow, in each dyed half of the channel. This is expressed as $u_f(y) = 6\overline{U}\left(\frac{y}{h}\right)\left(1 - \frac{y}{h}\right)$. The channel domain is discretized into a grid of 42,480 hexahedral cells, with approximately 360 cells along the channel length and 100 cells along its height. The thin plate structures are also discretized into a hexahedral grid, with 12 cells along the thickness and 50 cells along the height for each of the two plates. A detailed view of the domain mesh near the plates is shown in Figure 1. To determine the optimal grid size for our simulations, we performed a grid convergence analysis. We conducted a base simulation at $Re = 400$ under steady flow conditions past a single flexible plate $Sc = 10$. By increasing the resolution in each direction by a factor of 1.5, the total grid size became $480x177$ cells, effectively tripling the number of points. We observed that head loss and the mixing index showed insignificant variations, with changes amounting to no more than 1%. This indicated that the current grid size adequately resolves the flow and structural dynamics. Extensive grid refinement tests and validation studies on a similar simulation setup have been documented in our previous work (Singh and Lakkaraju, 2019a).

The velocity boundary conditions applied to the channel walls and flexible structure surfaces are no-slip and impermeable. At the channel outlet, the velocity gradients are set to zero, while the inlet velocity follows a parabolic inflow profile for both the top and bottom half, as previously described. The velocity at the interface between the solid structure and the fluid is the same, i.e., a no-slip boundary condition is used. Pressure boundary conditions are set to zero gradients at the channel walls, inlet, fluid-solid interface, and ambient pressure conditions at the outlet. Our study focuses on the streamwise location $x = 12h$, ensuring no boundary reflections and allowing properties to stabilize before exiting the channel.

3. Results

We have investigated the fluid mixing in a channel flow due to the passively oscillating flexible plates. According to Zhang et al. (2020), such plates subjected to an incoming flow may exhibit different deformation modes: lodging

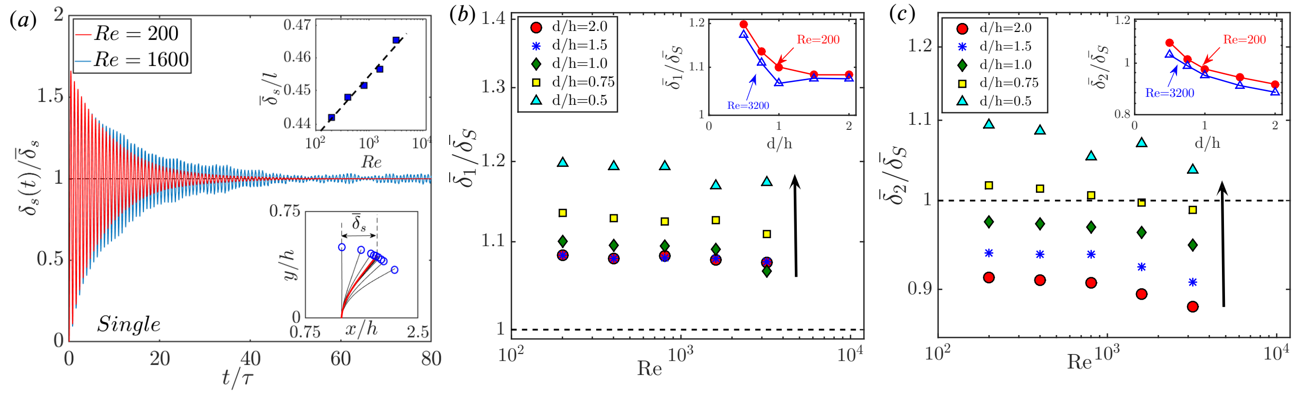

Figure 2: (a) Time history of the single plate tip deflection about steady state mean position for $Re = 200$ and 1600. A stroboscopic representation of the bending plate is shown in the inset figure, and the thick red plate marks the steady-state shape after deflection. (b) Tip deflection normalized by single plate mean deflection of plate 1 (upstream) and (c) plate 2 for different d/h configurations. The dashed line marks the single plate tip deflection for reference. The inset in each panel shows a tip deflection trend with d/h for $Re = 200$ and 3200.

mode, regular VIV mode (vortex-induced vibration or flutter), or static reconfiguration mode. Our parameter range places our cases in the phase space that shows static reconfiguration of the plates, as described in Zhang et al. (2020), where the plates align with the flow, reducing the projected area perpendicular to the flow and showing negligible flutter at steady-state.

To begin with, we studied the behavior of the flexible plates under the incoming flow. In Figure 2(a), we have shown the plates' flutter oscillation for the case where only a single plate is positioned at $2h$ length from the channel inlet. This plate reconfigures by bending in the streamwise direction by amplitude $\bar{\delta}_s$ and flutters around its mean position (shown as plate position in red in the subplot). The plates' flutter amplitude dampens down smoothly for $Re = 200$, unlike that in the high Re $(= 1600)$ case where the plates' flutter shows abrupt dampening due to flow features. We have also shown the mean plate deflection for increasing Re in the subplot, which shows a nearly linear trend in the semi-log plot. In the case with two wall-mounted plates arrangement, Figure 2(b) and (c) show steady state deflection amplitude for upstream plate $(\bar{\delta}_1)$ and for the downstream plate $(\bar{\delta}_2)$ normalized over the deflection amplitude in single plate case $(\bar{\delta}_S)$. We can observe that the $\bar{\delta}_1 > \bar{\delta}_S)$ for any Re and d/h case whereas $\bar{\delta}_2 > \bar{\delta}_S)\ for d/h > 0.8$. We have also shown the normalized plate deflection for d/h cases in the subfigures and found that the plate deflection increases with a decrease in d/h. We have thoroughly discussed the structural dynamics of the wall-mounted plates' such as damping, frequency, and deflection, in detail in our earlier work (Singh and Lakkaraju, 2019a).

The plates' deflection under the fluid load generates complex flow features due to the mutual interplay of forces. In Figure 3(a), we have shown instantaneous iso-contours of flow vorticity for single plate case at $Re = 200 - 3200$. The flow gets obstructed by the plate and accelerates through the remaining gap, generating vorticity at the top wall and in the form of the plate's tip-attached shear layer. We can notice the roll-up and breakdown of the shear layer upon increasing the Re beyond 200. The clockwise and counter-clockwise vortex structures generated off the plates' tip and the top wall, respectively, arrange themselves in alternating fashion downstream, which indicates periodic shedding of the vortices off the plate. These vortex structures, as they roll, advect downstream due to the incoming inertia and cause a stirring effect in the fluid, thereby causing the mixing of the two fluids.

In Figure 3(b), we have shown two scalar concentration fields $\phi = 0\&1$ initially separated distinctly into top-half and bottom-half, distinctly. For $Re = 200$, the instantaneous scalar field remains largely unmixed due to the flow disturbances as the single plate achieves static reconfiguration mode with negligible flutter amplitude, which does not impact the shear layer breakup. However, for $Re \geq 400$, we can observe a transition in the mixing of the scalar as the aforementioned vortices agitate the field more and more with increasing Re. These vortices entrain the scalar into their field and for localized mixing zones, increasing the mixing by diffusion. In the case with $Re = 3200$, we can note that the flow near the inlet also transitions towards a turbulent field even before interacting with the plates.

The mixing of the scalar field can be statistically evaluated by many methods used in the past (Danckwerts, 1952; Liscinsky et al., 1993; Kockmann et al., 2006). We have used the infamous statistical method for estimating mixing known as the 'Mixing Index, ' which in our work can be expressed along the channel downstream length as

$$MI(x) = 1 - \sqrt{\frac{\sigma(x)^2}{\sigma_{max}^2}},$$

$$where, \quad \sigma(x) = \sqrt{\frac{1}{h}\int_0^h [\phi(x,y) - \phi_m]^2\, dy}$$

where $\sigma(x)$ is the standard deviation of the vertically integrated scalar field across the channel, ϕ_m is the mean of the scalar concentration field or scalar concentration value for a

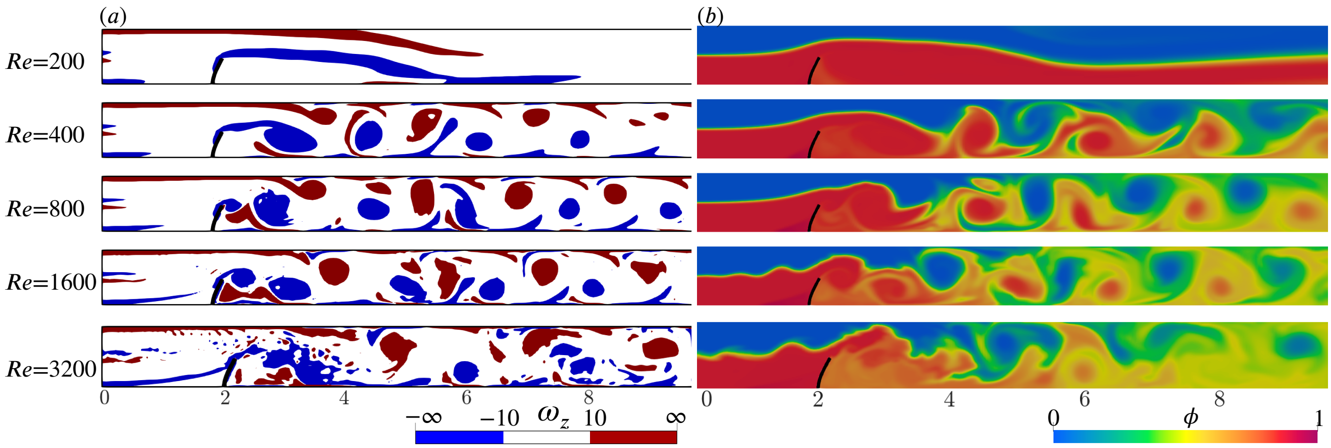

Figure 3: Instantaneous (a) iso-contours of spanwise vorticity (ω_z) and (b) scalar concentration field for single plate configuration case. The top-to-bottom panels are for Re = 200 to 3200.

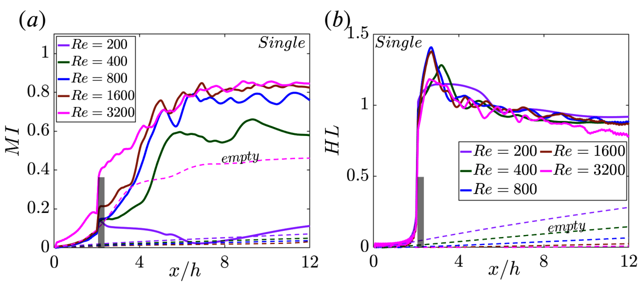

Figure 4: Time-averaged (a) mixing index MI and (b) head loss HL along the channel length downstream for a single flexible plate case for $Re = 200 - 3200$. The grey rectangle marks the location of plates in the channel. The dashed lines correspond to the empty channel case for respective Re as per the color code.

fully mixed solution, and σ_{max} is the maximum deviation in the scalar concentration field. According to this method, the 'Mixing Index' ranges from 0 to 1 where $MI = 1$ represents a completely mixed solution and $MI = 0$ represents the fully unmixed scalar field. We have accounted for a value-for-cost analogy in our work, where MI is considered the final value, which shall come at a cost. We have considered the head loss in the channel flow caused by the presence of flexible obstructions as the cost for the value. We have computed head loss along the channel by vertically (across the channel length) integrating the mechanical head along the channel and subtracting from the initial pressure, which is expressed as:

$$\mathcal{H}^*(x) = \frac{\mathcal{H}(x)}{\rho_f \overline{U}^2}; \quad \mathcal{H}(x) = \frac{1}{h}\int_0^h [p(x,y) + \frac{1}{2}u_f^2(x,y)]\,dy$$

$$Head\ Loss, HL(x) = \mathcal{H}^*(0) - \mathcal{H}^*(x)$$

In Figure 4(a), we show $MI(x)$ for the single plate case for different Re. The grey rectangle in the figure marks the streamwise position of the plate in the channel for reference. As suggested in the contour plots, we see that mixing for $Re = 200$ case is much lower than the higher Re cases. For $Re \geq 400$, the MI shoots high in the channel downstream as early as $x = 5h$. We have also simulated an empty channel flow, i.e., no obstruction, with the same scalar field configuration for the Re range for reference. The dashed curves in the plot show MI for the empty channel case following the same color codes for the Re case. We can notice that the $MI(x)$ in an empty channel follows a linear trend for $Re \leq 1600$, whereas in the case with $Re = 3200$, the flow destabilizes into the transition zone, and a non-linear $MI(x)$ curve can be observed.

In Figure 4(b), we have shown the total mechanical head loss, HL, for a single plate case along the channel streamwise direction for varying Re. The HL spikes up near the plate due to the sudden obstruction of the flow inertia and then decays to a nearly constant value as the flow improves downstream. Despite the difference in MI for varying Re, HL value does not vary significantly with Re near the exit. We have also shown HL for the empty channel case for reference, and an increasing slope in the linear trend can be observed for decreasing Re.

With an initial analysis of the single plate case, we extend our study further by introducing the second plate downstream. In figure 5(a), instantaneous vorticity iso-contours are shown for single and two plate configurations with $d/h = 2, 1.5, 1, 0.5, 0$ at $Re = 400$. The presence of another plate contributes to more vorticity than the single plate case as plate 2 assists the top wall shear layer to shed periodically of its tip. When plate 2 is placed even closer, the vortex shedding off both plates' tips is more frequent and intense because of its effective flow blockage. In figure 5(b), the instantaneous contour for the scalar field is shown for the same set of configurations at $Re = 800$. In a single plate case, the flow jumps over the plate, destabilizes, and, in turn, agitates further downstream. With the placement of the second plate on the opposite wall, this flow jump gets constricted as per the location of plate 2, and thus, we can notice the early blending of the two fluids as d/h is decreased. Note that, in $d/h = 0$ configuration, the two plates heavily obstruct the flow, disturb the flow even

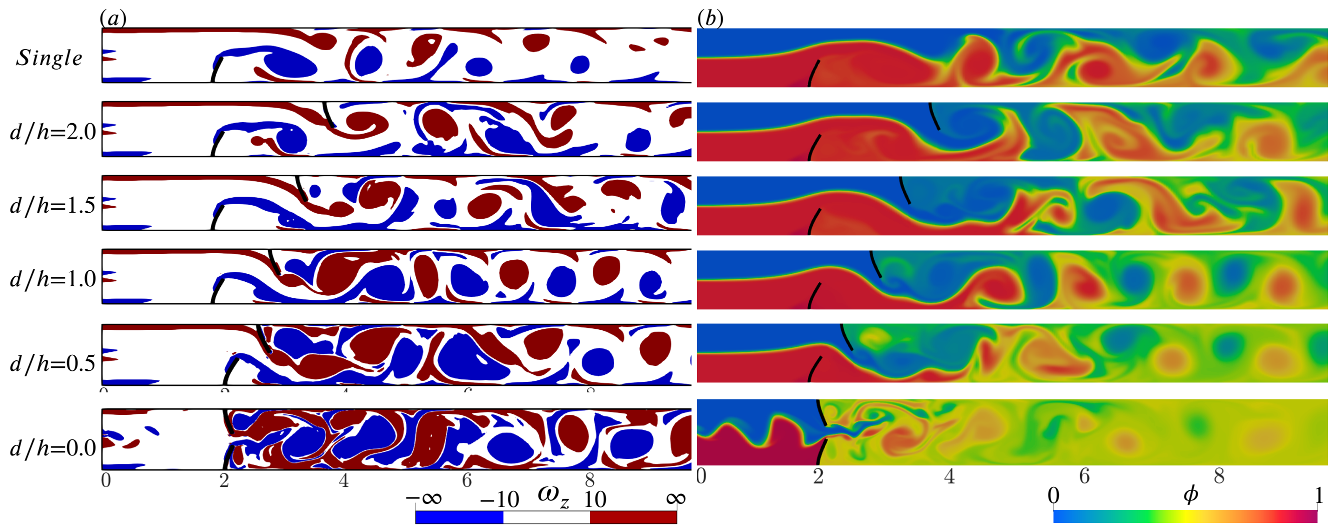

Figure 5: Instantaneous (a) iso-contours of spanwise vorticity (ω_z) and (b) scalar concentration field for Re = 800 case. The top-to-bottom panels are for different d/h configurations.

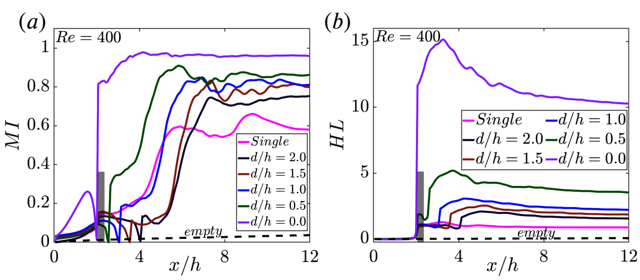

Figure 6: Time-averaged (a) mixing index MI and (b) head loss HL along the channel length in the downstream for single and two plate cases with different d/h configurations at Re = 400. The grey rectangle marks the location of plates in the channel. The dashed lines correspond to the empty channel case for respective Re as per the color code.

upstream to the plates, and induce slight fluid mixing before the obstruction.

In Figure 6(a), MI along channel length for the various d/h configurations is compared for Re = 400 in steady state. As evident by the contour plots before, the MI in the channel shoots up steeply past the plates' location. The grey rectangle marks the location of plate 1 in the channel for reference. We observe that MI at further downstream locations subsequently decreases with increasing d/h with maximum value at d/h = 0, showing significant mixing ahead of the plates and peak mixing immediately next to the plates. However, this steep mixing curve for d/h = 0 configuration comes at a high head loss, as shown in figure 6(b), which features a significant difference from the other configurations. The plot shows expected head loss results as per the flow obstruction configuration, i.e., decreasing HL with increasing plates' separation (d/h).

For a comprehensive overview of the development of MI for different configurations under various Re, we have shown the time-space plots in figure 7. This reveals that at lower Re, the MI increases gradually over time, whereas at higher Re, we can see early mixing of fluids also increased mixing as the d/h decreases. However, the d/h = 0 configuration stands out with the highest mixing very early in the channel as well as early in time. Interestingly, the Re = 800 case exhibits much better mixing results than the Re = 3200 case for d/h = 0.

In Figure 8(a), we have summarised the mixing performance of all the cases studied in our work. We have shown MI and HL attained at the channel length x = $12h$ (out of $14h$ length) for cases with different d/h and Re. The data points are clustered according to the Re for each d/h configuration, and the dotted connecting lines are marked only to show the collection and reflect no trend whatsoever. A zoomed-up version of the figure is attached in the Appendix section for details on Re correspondence with the marker point. The data cluster with dark asterisk markers is shown for an empty channel, which results in a reference and relative comparison. The overall data reiterates our finding that the HL increases significantly upon decreasing d/h. However, MI shows results nearly similar for $Re \geq 200$ with d/h = 0 case as an exception, which stands out in mixing value but with increased HL as cost.

When designing a fluid channel mixer, a key objective is to make it as compact as possible while maintaining effective mixing. To assess the "compactness" of a channel mixer with wall-mounted plates, we compare it to an empty channel (one without plates) to determine how long the empty channel would need to be to achieve the same level of mixing as the channel with plates at the streamwise location x/h = 12. Similarly, we evaluate efficiency losses by finding the length of an empty channel that experiences the same pressure loss as a channel with plates. These equivalent lengths for the empty channel are quantified separately for mixing length (E_M) and head loss (E_H). To estimate these equivalent lengths, we observe that the mixing index and head loss in an empty channel with steady inlet flow (i.e.,

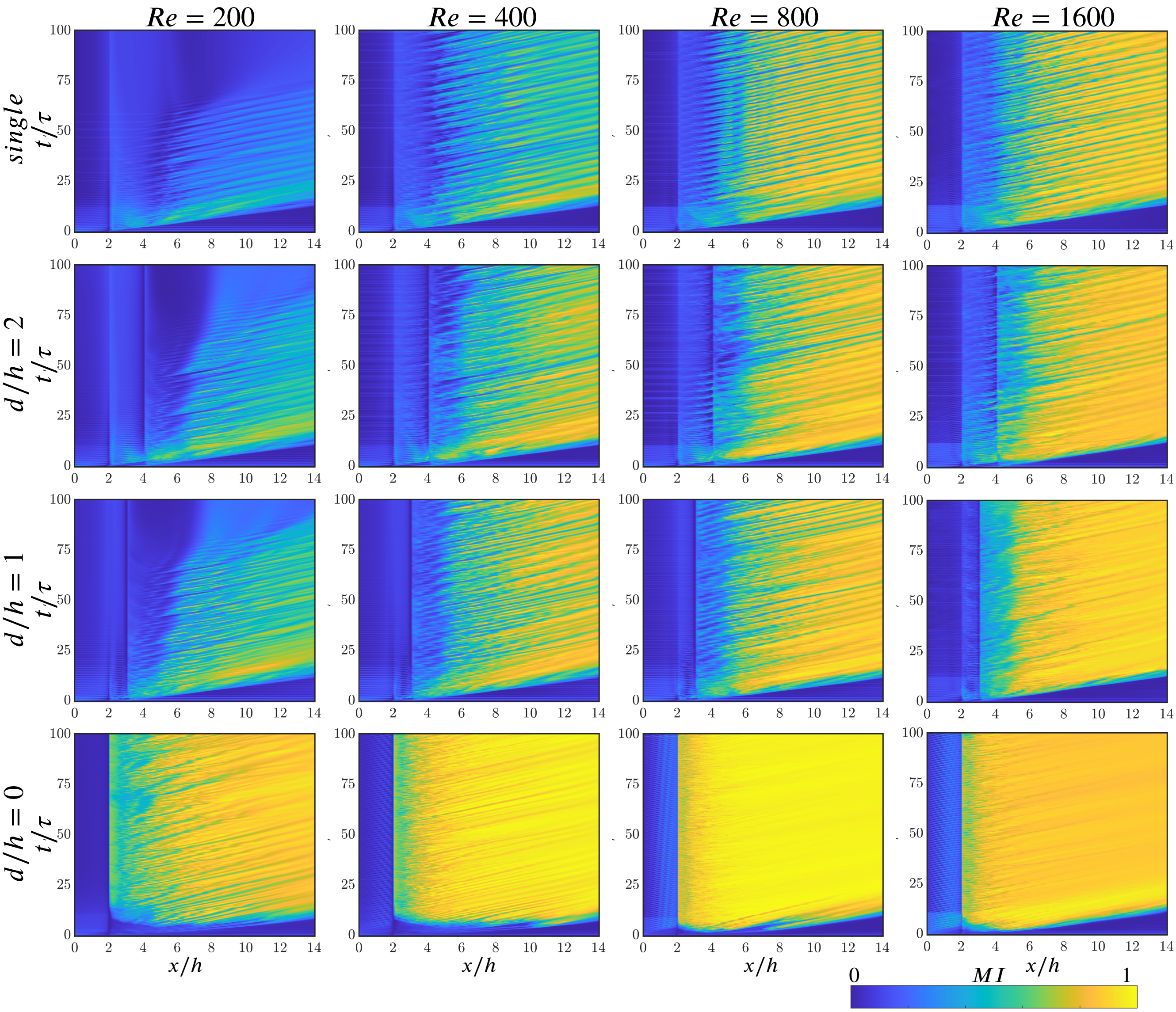

Figure 7: Timespace map for mixing index (MI) for single and $d/h = 0, 1, 2$ cases (row-wise), and for $Re = 200, 400, 800, 1600$ cases (column-wise).

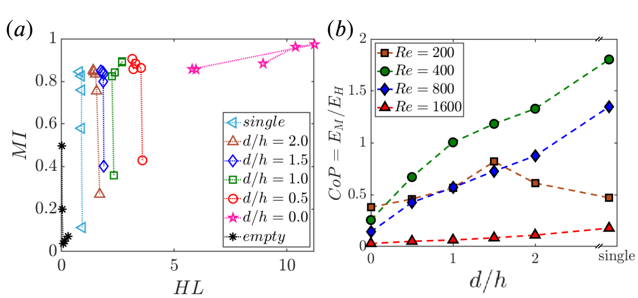

Figure 8: (a) Comprehensive map of all the cases considered in our work in terms of mixing index MI and head loss HL. The asterisk mark corresponds to the steady inlet flow case. A zoom-in of each cluster based on the plates' flexibility is shown separately in the Appendix section. (b) Coefficient of performance CoP for different plate configuration cases at $Re = 200 - 1600$.

no plates) can be accurately fit as linear profiles, which for different Re are as:

$$
\begin{aligned}
Re = 200 \quad & MI = 0.0015x/h \quad HL(x) = 0.0604x/h \\
Re = 400 \quad & MI = 0.011x/h \quad HL(x) = 0.0301x/h \\
Re = 800 \quad & MI = 0.0082x/h \quad HL(x) = 0.0131x/h \\
Re = 1600 \quad & MI = 0.0024x/h \quad HL(x) = 0.0046x/h
\end{aligned}
$$

Using this information, we introduce a Coefficient of Performance (CoP) for the mixer, calculated as the ratio of equivalent lengths for mixing and loss, i.e., $CoP = E_M/E_H$ (Rips and Mittal, 2019; Singh et al., 2024). This coefficient allows us to measure how much the mixing improves relative to the increase in efficiency loss for a mixer with plates compared to one without any plate. Figure 8(b) shows the CoP for various d/h cases at different flow Re. We find that the CoP increases with d/h with maximum performance in the case of a single plate in the channel. Also, the plot suggests that the $Re = 400$ allows the best operating conditions for the fluid mixing processes. Notably, at low

$Re(= 200)$, plates' configuration with $d/h = 1.5$ serves the best mixing performance.

4. Summary

We conducted numerical simulations to study the mixing in a channel that is set to be filled with fluid of two different scalar concentration fields, which are initially separated along the channel length flow at different Re with a range of $200 - 3200$. We introduced two flexible plates anchored to the channel walls alternately at varying separation distances $d/h = 0, 0.5, 1, 1.5, 2$ and investigated the mixing performance due to the fluid-structure interaction. The flexible plates bend under the flow inertia and oscillate around a mean reconfigured position, which causes vortex shedding off each plate's tip and contributes to the intermixing of the two scalar fields. We used standard metrics to evaluate both the mixing efficiency and the resulting mechanical head loss for the cost-to-value analogy.

Our key findings indicate that the $d/h = 0$ configuration of the two plates in the channel stands out and results in a maximum mixing effect for any Reynolds number category. The mixing, in this case, is also much earlier in the channel, i.e., immediately next to the plates' position and also early in time. However, the plates' arrangement causes maximum obstruction to the flow and thus results in high pressure head loss. An overall map of rest all the plate configurations reveals that the decrease in d/h causes the increased head losses but does not contribute to the mixing significantly in flow conditions $Re \geq 400$. To comprehensively assess mixing performance, considering both mixing quality and head loss, we compared our configuration with an empty channel (no obstacles). We used equivalent empty channel lengths (E_M and E_H) for this comparison, aiming to match the metrics of the channel with plates. We then calculated the coefficient of performance, defined as $CoP = E_M/E_H$, for all scenarios to rank our setups based on their mixing performance. The highest mixing performance (CoP) is observed for single plate configuration because it features considerably low head loss in the channel flow. We also found that the $Re = 400$ flow condition is best suited for high mixing CoP. At low Re (= 200) in our case, the $d/h = 1.5$ configuration resulted in the highest mixing performance. However, our study has limitations. The channel mixer design used is simple, representing a straight, two-dimensional channel. In practical applications, mixers might feature more complex, duct-like channels where three-dimensional flow dynamics are significant. These three-dimensional aspects could affect the behavior of the elastic plates and overall flow dynamics. Future research could investigate the impact of plate geometry and its placement within the channel on mixing efficiency.

5. Acknowledgement

We thank our fellow members of TuRbulent Interfaces And Dispersion (TRIAD), IIT Kharagpur, for their support. We acknowledge research grants from the Board of Research and Nuclear Science(BRNS), INSPIRE, and MATRICS sponsored by the Science and Engineering Research Board of the Government of India. We sincerely thank Param Shakti for computing resources developed under the National Supercomputing Mission at IIT Kharagpur, India.

References

Abdelhamid, T., Alam, M.M., Islam, M., 2021. Heat transfer and flow around cylinder: Effect of corner radius and reynolds number. Int. J. Heat Mass Transf. 171, 121105.

Alben, S., Shelley, M., 2008. Flapping states of a flag in an inviscid fluid: Bistability and the transition to chaos. Phys. Rev. Lett. 100, 74301.

Ali, S., Habchi, C., Menanteau, S., Lemenand, T., Harion, J.L., 2015. Heat transfer and mixing enhancement by free elastic flaps oscillation. Int. J. Heat Mass Transf. 85, 250–264.

Ali, S., Menanteau, S., Habchi, C., Lemenand, T., Harion, J.L., 2016. Heat transfer and mixing enhancement by using multiple freely oscillating flexible vortex generators. Appl. Therm. Eng. 105, 276–289.

Bagheri, S., Mazzino, A., Bottaro, A., 2012. Spontaneous symmetry breaking of a hinged flapping filament generates lift. Physical Review Letters 109, 154502.

Borazjani, I., Sotiropoulos, F., 2009. Vortex-induced vibrations of two cylinders in tandem arrangement in the proximity–wake interference region. Journal of Fluid Mechanics 621, 321–364. doi:10.1017/S0022112008004850.

Campbell, R.L., Paterson, E., 2011. Fluid–structure interaction analysis of flexible turbomachinery. Journal of Fluids and Structures 27, 1376–1391.

Chen, Y., Ryu, J., Liu, Y., Sung, H.J., 2020. Flapping dynamics of vertically clamped three-dimensional flexible flags in a poiseuille flow. Phys. Fluids (1994) 32, 071905.

Dadvand, A., Hosseini, S., Aghebatandish, S., Khoo, B.C., 2019. Enhancement of heat and mass transfer in a microchannel via passive oscillation of a flexible vortex generator. Chem. Eng. Sci. 207, 556–580.

Danckwerts, P.V., 1952. The definition and measurement of some characteristics of mixtures. Flow Turbulence and Combustion 3, 279–296.

Eizadi, H., An, H., Zhou, T., Zhu, H., Cheng, L., 2022. Wake transitions of six tandem circular cylinders at low reynolds numbers. Phys. Fluids (1994) 34, 023605.

Eloy, C., Lagrange, R., Souilliez, C., Schouveiler, L., 2008. Aeroelastic instability of cantilevered flexible plates in uniform flow. Journal of Fluid Mechanics 611, 97–106.

Favier, J., Revell, A., Pinelli, A., 2015. Numerical study of flapping filaments in a uniform fluid flow. Journal of Fluids and Structures 53, 26–35.

Hemati, M.S., Williams, M.O., Rowley, C.W., 2014. Dynamic mode decomposition for large and streaming datasets. Physics of Fluids 26, 111701.

Holmes, P., Lumley, J.L., Berkooz, G., 1996. Turbulence, coherent structures, dynamical systems and symmetry. Cambridge Monographs on Mechanics , 20–85.

Hosseini, S., Aghebatandish, S., Dadvand, A., Khoo, B.C., 2021. An immersed boundary-lattice boltzmann method with multi relaxation time for solving flow-induced vibrations of an elastic vortex generator and its effect on heat transfer and mixing. Chem. Eng. J. 405, 126652.

Hsiao, K.Y., Wu, C.Y., Huang, Y.T., 2014. Fluid mixing in a microchannel with longitudinal vortex generators. Chem. Eng. J. 235, 27–36.

Huera-Huarte, F., Gharib, M., 2011. Vortex- and wake-induced vibrations of a tandem arrangement of two flexible circular cylinders with far wake interference. Journal of Fluids and Structures 27, 824–828. doi:https://doi.org/10.1016/j.jfluidstructs.2011.02.006. iUTAM Symposium on Bluff Body Wakes and Vortex-Induced Vibrations (BBVIV-6).

Jeong, J., Hussain, F., 1995. On the identification of a vortex. Journal of Fluid Mechanics 285, 69–94.

Jin, Y., Kim, J.T., Mao, Z., Chamorro, L., 2018. On the couple dynamics of wall-mounted flexible plates in tandem. Journal of Fluid Mechanics

852, R2.

Jing, D., Zhan, X., 2022. Numerical studies on the hydraulic and mixing performances of fluid flow around a cylinder in microchannel with vertical flexible flag. Chem. Eng. J. 430, 133009.

Kang, D., 2015. Effects of baffle configuration on mixing in a T-shaped micro-channel. Micromachines 6, 765–777. doi:10.3390/mi6060765.

Kashid, M., Renken, A., Kiwi-Minsker, L., 2011. Mixing efficiency and energy consumption for five generic microchannel designs. Chemical Engineering Journal 167, 436–443.

Kevlahan, N., C. R. Hunt, J., Vassilicos, J., 1994. A comparison of different analytical techniques for identifying structures in turbulence. Applied Scientific Research 53, 339–355.

Khatavkar, V.V., Anderson, P.D., den Toonder, J.M.J., Meijer, H.E.H., 2007. Active micromixer based on artificial cilia. Phys. Fluids (1994) 19, 083605.

Kockmann, N., Kiefer, T., Engler, M., Woias, P., 2006. Convective mixing and chemical reactions in microchannels with high flow rates. Sensors and Actuators B: Chemical 117, 495–508.

Liscinsky, D., True, B., Holdeman, J., 1993. Experimental investigation of crossflow jet mixing in a rectangular duct .

van Loon, R., Anderson, P.D., van de Vosse, F.N., Sherwin, S.J., 2007. Comparison of various fluid–structure interaction methods for deformable bodies. Comput. Struct. 85, 833–843.

Mehendale, N., Sharma, O., Pandey, S., Paul, D., 2018. Clogging-free continuous operation with whole blood in a radial pillar device (rapid). Biomedical Microdevices 20.

Nguyen, N.T., Wu, Z., 2005. Micromixers– a review. Journal of Micromechanics and Microengineering 15, 1–16. doi:10.1088/0960-1317/15/2/R01.

Nguyen, V.T., 2010. An arbitrary Lagrangian–Eulerian discontinuous Galerkin method for simulations of flows over variable geometries. Journal of Fluids and Structures 26, 312–329.

Núñez-Flores, A., Sandoval, A., Mancilla, E., Hidalgo-Millán, A., Ascanio, G., 2020. Enhancement of photocatalytic degradation of ibuprofen contained in water using a static mixer. Chem. Eng. Res. Des. 156, 54–63.

Park, J.W., Ryu, J., Sung, H.J., 2019. Effects of the shape of an inverted flag on its flapping dynamics. Phys. Fluids (1994) 31, 021904.

Peterwitz, M., Schembecker, G., 2021. Evaluating the potential for optimization of axial back-mixing in continuous pharmaceutical manufacturing. Comput. Chem. Eng. 147, 107251.

Pfister, J.L., Marquet, O., 2020. Fluid–structure stability analyses and nonlinear dynamics of flexible splitter plates interacting with a circular cylinder flow. J. Fluid Mech. 896.

Rips, A., Mittal, R., 2019. Flutter-enhanced mixing in small-scale mixers. Physics of Fluids 31, 107107. doi:10.1063/1.5115351.

Sadatoshi, T., 1968. Waving motions of flags. Journal of the Physical Society of Japan 24, 392–401.

Saleh, H., Siri, Z., Hashim, I., 2019. Role of fluid-structure interaction in mixed convection from a circular cylinder in a square enclosure with double flexible oscillating fins. Int. J. Mech. Sci. 161-162, 105080.

Singh, G., Lakkaraju, R., 2019a. Wall-mounted flexible plates in a two-dimensional channel trigger early flow instabilities. Phys. Rev. E 100, 023109.

Singh, G., Lakkaraju, R., 2019b. Wall-mounted flexible plates in a two-dimensional channel trigger early flow instabilities. Phys. Rev. E. 100, 023109.

Singh, G., Senapati, A., Sharma, A., Atta, A., Lakkaraju, R., 2024. Flexible structures enhance fluid mixing in a channel flow. Physics of Fluids 36, 024103. doi:10.1063/5.0186196.

Slone, A.K., Pericleous, K., Bailey, C., Cross, M., 2002. Dynamic fluid–structure interaction using finite volume unstructured mesh procedures. Computers & Structures 80, 371–390.

Squires, T.M., Quake, S.R., 2005. Microfluidics: Fluid physics at the nanoliter scale. Rev. Mod. Phys. 77, 977–1026.

Stroock, A., K. W. Dertinger, S., Ajdari, A., Mezic, I., A. Stone, H., M. Whitesides, G., 2002. Chaotic mixer for microchannels. Science 295, 647–651.

Tukovic, Z., Jasak, H., 2007. Updated lagrangian finite volume solver for large deformation dynamic response of elastic body. Transactions of FAMENA 31, 55.

Vandenberghe, N., Zhang, J., Childress, S., 2004. Symmetry breaking leads to forward flapping flight. Journal of Fluid Mechanics 506, 147–155.

Wang, J., Zhen, Y., 2021. Application and patent of static mixer in plastic processing. Recent Pat. Mech. Eng. 14, 94–104.

Wang, L., Zhou, Y., 2018. Two tandem cylinders of different diameters in cross-flow: Effect of an upstream cylinder on wake dynamics. Journal of Fluid Mechanics 836, 5–42. doi:10.1017/jfm.2017.735.

Wang, S., Ryu, J., Yang, J., Chen, Y., He, G.Q., Sung, H.J., 2020. Vertically clamped flexible flags in a poiseuille flow. Phys. Fluids (1994) 32, 031902.

Ward, K., Fan, Z.H., 2015. Mixing in microfluidic devices and enhancement methods. Journal of micromechanics and microengineering : structures, devices, and systems 25. URL: https://www.mdpi.com/2072-666X/8/9/274.

Watanabe, Y., Suzuki, S., Sugihara, M., Sueoka, Y., 2002. An experimental study of paper flutter. Journal of Fluids and Structures 16, 529–542.

Yadav, P.K., Sourav, K., Kumar, D., Sen, S., 2021. Flow around a diamond-section cylinder at low reynolds numbers. Phys. Fluids (1994) 33, 053611.

Yang, A.S., Chuang, F.C., Chen, C.K., Lee, M.H., Chen, S.W., Su, T.L., Yang, Y.C., 2015. A high-performance micromixer using three-dimensional tesla structures for bio-applications. Chem. Eng. J. 263, 444–451.

Yeh, S.I., Sheen, H.J., Yang, J.T., 2015. Chemical reaction and mixing inside a coalesced droplet after a head-on collision. Microfluid. Nanofluidics 18, 1355–1363.

Yu, Y., Liu, Y., Chen, Y., 2017. Vortex dynamics behind a self-oscillating inverted flag placed in a channel flow: Time-resolved particle image velocimetry measurements. Phys. Fluids (1994) 29, 125104.

Zhang, J., Childress, S., Libchaber, A., Shelley, M., 2001. Flexible filaments in a flowing soap film as a model for one-dimensional flags in a two-dimensional wind. Nature 408, 835–839.

Zhang, X., He, G., Zhang, X., 2020. Fluid–structure interactions of single and dual wall-mounted 2d flexible filaments in a laminar boundary layer. Journal of Fluids and Structures 92, 102787.

Zhao, M., 2020. Effects of natural frequency ratio on vortex-induced vibration of a circular cylinder in steady flow. Phys. Fluids (1994) 32, 073604.

Zhu, L., Peskin, C.S., 2002. Simulation of a flapping flexible filament in a flowing soap film by the immersed boundary method. Journal of Computational Physics 179, 452–468.

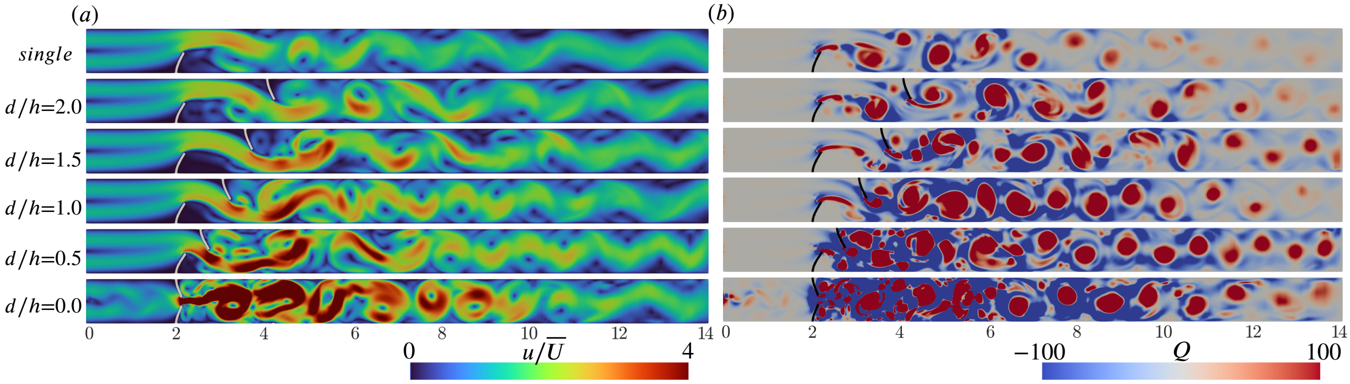

Figure 9: (a) Instantaneous velocity contour for different cases. (b) Q-criterion based vortex structures are shown. Both cases correspond to $Re = 400$

Appendix

In our investigation, We employed advanced visualization techniques to understand the dynamics at play. Figure 9 illustrates the instantaneous velocity contour (left) and Q-criterion-based vortex structures. The Q-criterion is a method for identifying strong vortices in the flow; Zones dominated by vortices are identified by $Q > 0$, while strained zones are indicated by $Q < 0$ (Kevlahan et al., 1994; Jeong and Hussain, 1995; Holmes et al., 1996; Hemati et al., 2014). We observed that the flow velocity speeds up as the plates' constriction is reduced with decreasing d/h. The compliance of flow with plate 1 and plate 2 causes the flow to meander in a wave-like form downstream. We also observe an increasing number of vortex structures along the channel length with decreasing plates' separation d/h.

Figure 10 provides the time evolution of the MI for $Re = 400$ case for different plates' configuration cases. We notice the earliest fluid mixing for the $d/h = 0$ case, whereas the single plate case takes more time to reach its respective MI maximum. In Figure 11, we zoomed in into clusters of data points shown in figure 8(a) so to better understand the effects of Re on the overall mixing efficiency vs head loss map

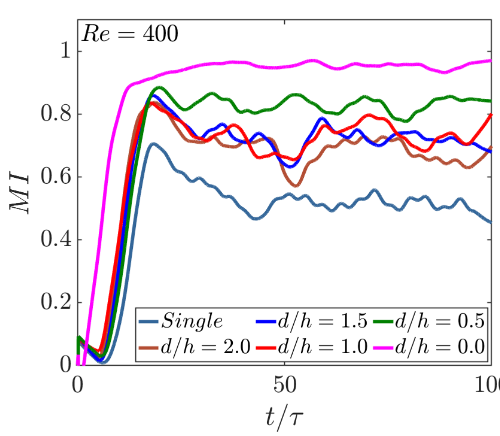

Figure 10: Time evolution of mixing index MI near the channel exit at the length $x = 12h$ along the channel length in the downstream for single and two plate case with different d/h configurations at $Re = 400$.

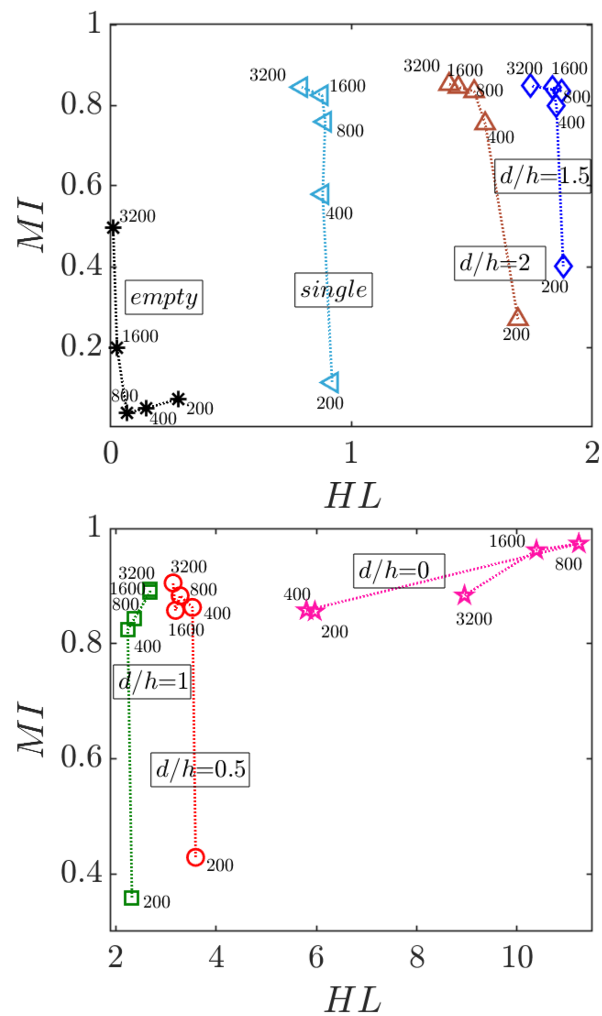

Figure 11: Zoom-in of clusters of data points shown in Figure 8(a). Re value is shown near each data point.